Fine microstructure of high performance electrode in alkaline anion exchange membrane fuel cells

Donglei Yang [a,b,c], Hongmei Yu [a,b,*], Guangfu Li [a,b], Yun Zhao [a,b], Yanxi Liu [a,b], Changkun Zhang [a,b,c], Wei Song [a,b], Zhigang Shao [a,b]

[a] Dalian National Laboratory for Clean Energy, Dalian 116023, China
[b] Dalian Institute of Chemical Physics, Chinese Academy of Sciences, Dalian 116023, China
[c] University of the Chinese Academy of Sciences, Beijing 100039, China

HIGHLIGHTS

- Microstructure of electrode with anion-exchange ionomer is studied and improved.
- The colloidal anion-exchange ionomer is prepared and evaluated for the first time.
- A high performance of 407 mW cm^{-2} in the alkaline fuel cell is obtained.

GRAPHICAL ABSTRACT
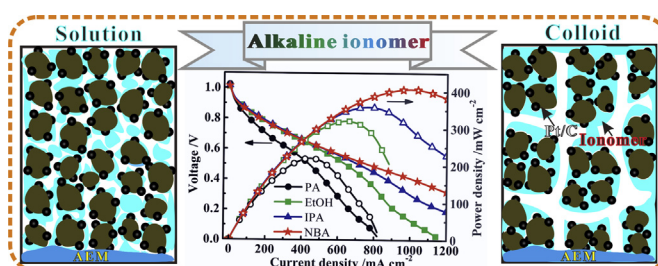
ARTICLE INFO

ABSTRACT

The electrode fabrication and resulting microstructure are the main determinates of the performance of alkaline anion exchange membrane fuel cells (AAEMFCs). In the present work, the electrode microstructure is adjusted by the ionomer content in catalyst layers as well as the dispersion solvent for catalyst inks. The ionomer content shows a strong influence on the cell active, ohmic and mass-diffusion polarization losses. Especially, an in-suit proof for the ionomer as the hydroxide conductor is first given by the cell cycle voltammogram, and the optimum content is 20 wt.%. Meanwhile, it is found that the ionomer either dissolves in the dielectric constant $\varepsilon = 18.3$–24.3 solutions (including ethanol, propanol and isopropanol) or disperses in the n-butyl acetate ($\varepsilon = 5.01$) colloid. Compared with these electrodes using the solution method, the colloidal electrode tends to form the larger catalyst/ionomer agglomerates, increased pore volume and pore diameter, continuous ionomer networks for hydroxide conduction, and correspondingly decreased ohmic and mass-diffusion polarization losses. Ultimately, when employing the optimum ionomer content and the colloid approach, the highest peak power density we achieved in AAEMFC is 407 mW cm^{-2} at 50 °C, which can be taken as a considerable success in comparison to the current results in publications.

© 2014 Elsevier B.V. All rights reserved.

1. Introduction

Alkaline anion exchange membrane fuel cell (AAEMFC) using a solid polymer membrane to replace the liquid caustic alkaline electrolyte, has been undergoing revolutionary developments in recent decades [1–3]. Compared with the proton exchange

* Corresponding author. Dalian Institute of Chemical Physics, Chinese Academy of Sciences, Dalian 116023, China.
E-mail address: hmyu@dicp.ac.cn (H. Yu).

membrane fuel cell (PEMFC), AAEMFC has emerged some outstanding advantages to overcome the technical and cost issues, including the faster electrochemical reaction kinetics of both the fuel oxidation and oxygen reduction reaction, minimized corrosion issues, decreased fuel crossover rates and potentially improved water management, etc [1,4—9]. In particular, the fast reaction kinetics can reduce or remove the demand for noble metal electrocatalysts like platinum-based catalysts [2,7,10]. To fully realize these advantages, enormous efforts have been put into the research and development of AAEMFC. Unfortunately, the use of anion exchange membranes (AEMs) brings about new electrode design and assembly challenges, and the cell performance has not yet been satisfactory for the industrial and commercial application [1,11]. One of the major reasons is attributed to the lagging development of efficient membrane electrode assemblies (MEAs) due to the challenge in yielding optimal accessibility, stability and numbers of three phase boundaries (TPBs) where the catalysts, ionomers and reactants meet and react [9,12—16]. To build ideal TPBs and electrode architectures, the fabricated MEAs require a combination of high catalyst utilization, sufficient ion conduction, and flexible reactant and product transport in the CLs [17]. Research on advanced MEA design and preparation should be necessary to make the performance break through.

The MEA as the fuel cell's heart is typically composed of an AEM, catalyst layers (CLs) and gas diffusion layers [18]. Currently, the state-of-the-art method for creating the CLs is the catalyst coated membrane (CCM) where CLs are formed by directly coating catalyst slurry on both sides of the AEM. Its advantage over the traditional catalyst-coated gas diffusion electrode is the incorporation of more catalyst particles into the solid electrolyte media, where hydroxide are more easily to transport from the cathode to the anode [19]. The CLs play critical roles of reducing the reaction activation barrier as well as cost for fuel cell [20]. The catalyst slurry used to fabricate CLs is usually constituted of catalyst nanoparticles mixed with ionomer/binder and dispersion solvent. In a traditional PEMFC system, the use of Nafion ionomer in CLs can extend the TPBs of catalytic reaction. The Nafion ionomer serves as the physical binder and proton conductor in the porous CLs, and the molecular interaction between the catalyst particles and ionomer will play a significant role in governing the final microstructure and properties of the MEA [14,21—23]. However, the excessive ionomer enriched in the CL surface will cause a negative impact on the electrochemical reaction due to high shielding of Pt-based particles and the increased limitations of the reactant, product and electron transport [21]. Therefore, the optimization of the ionomer content is a critical step in achieving high-performance MEAs. Besides, in our previous work, the commercial anion-exchange ionomer AS-4 was identified with the high hydroxide conductivity and good stability in the AAEMFC using our home-made AEM [24].

As a matter of fact, it is known that the dispersion solvent for the catalyst ink controls the ionomer molecular morphology in solution and thus determines the final microstructure of ionomer in the CLs [25,26]. The low-boiling solvents such as ethanol (EtOH), propanol (PA) and isopropanol (IPA) are frequently used to dissolve the alkaline ionomer commonly with the quaternary ammonium hydroxide [24,27,28]. In the meantime, it was reported that the dielectric constant (ε) of the organic dispersion solvent determines the state of the Nafion ionomer used in PEMFCs, including solution when $\varepsilon > 10$, colloid when $3 < \varepsilon < 10$ and precipitate when $\varepsilon < 3$, respectively [25,29—31]. This is because the ε value of a solvent molecule strongly relates to its polarizability, and characterizes the solvation and dispersibility to molecules/ions of another substance like ionomer. It is interested to note that ionomer dispersion states adjusted by the solvent' ε can change the shapes of double layer region on catalyst surface and eventually influence the charge

transfer process [32,33]. However, the alkaline system with the anion-exchange ionomer is significantly different from the acidic PEM system with the Nafion ionomer due to the varied ionomers and membranes [1]. Additionally, some other properties of dispersion solvents, such as boiling point, relative volatilization rate and viscosity, also may cause a formidable influence on the electrode microstructure.

In the current study, we seek to investigate and understand the influences of the ionomer content in CLs and the dispersion solvents for the catalyst slurry on the electrode microstructure and corresponding performance. Using the optimized fabrication approach, our results indicated that the prepared electrode with improved microstructure obtained significantly high performance in AAEMFC.

2. Experimental

2.1. MEA fabrication

To prepare a CCM, the commercial 70 wt. % Pt/C particles (Johnson Matthey), 5 wt.% As-4 solution (Tokuyama Corp.) and A-201 membrane (Tokuyama Corp.) were supplied as the electrocatalysts (both in the anode and the cathode), alkaline ionomer and AEM, respectively. Catalyst inks composed of the electrocatalyst, ionomer and dispersion solvent were homogenized for 1 h in an ultrasonic bath. The resulting inks were then sprayed onto both sides of the AEM. The Pt loading measured by weighting was about 0.4 mg cm^{-2} on each side including the anode and cathode. The ionomer content which was equal on each side was described as the dry weight proportion of the ionomer to the whole CL. Two pieces of carbon paper (Toray, TGP-H-060) were utilized as the anode and cathode gas diffusion layer, respectively. MEAs were prepared by hot-pressing the sandwich of the CCM and the gas diffusion layers at 60 °C and 1 MPa for 2 min.

2.2. Characterization of CL microstructure

The surface morphology of the prepared CCMs was observed by the scanning electron microscope (SEM, JOEL JSM-7800F) with an accelerated voltage of 5 kV. The pore structures of electrodes were measured by the mercury intrusion porosimetry (MIP) with a Quantachrome PoremasterGT 60. The test pressure ranged from 200 psi to 30000 psi and the mercury contact angle was 140°.

2.3. Single cell tests

The prepared MEAs were assembled into fuel cells designed with an effective area of 5 cm^2. Fuel cell test were conducted at 50 °C by passing H$_2$/O$_2$ (100% relative humidity, RH) with the flow rate of 100/200 mL min^{-1} at 0.05 MPa, respectively. The i–V curves, high-frequency resistance (R_{HF}) and in-situ electrochemical impedance spectroscopy (EIS) spectra of single cells were measured and recorded by an electric load system (KMF2030, Kikusui Electronics Corp.). The EIS experiments were carried out at a current density of 100 mA cm^{-2} with a small—amplitude alternating current of 10 mA cm^{-2} and the frequency range was from 0.1 Hz to 10 kHz.

After the EIS test, the in-suit cell cyclic voltammogram (CV) was collected at 50 mV s^{-1} and 50 °C between 0 V and 1 V to monitor the function of alkaline ionomer content in CLs. H$_2$ gas (100% RH, 100 mL min^{-1}) was supplied to the anode as counter electrode and reference electrode, and N$_2$ gas (100% RH, 300 mL min^{-1}) was fed into the cathode as working electrode.

3. Results and discussion

To illustrate the work principle, Fig. 1(a) presents a schematic of a typical AAEMFC (H_2 as the fuel and O_2 as the oxidant). Under the operation conditions, the hydroxide ions are generated by the catalytic oxygen reduction reaction in the cathode TPBs (Fig 1(c).), and then transported through the AEM to the anode TPBs (Fig 1(b)) where hydroxide ions react with H_2 to produce H_2O and electrons. For the cell reaction to continue, not only the number of TPBs is important but also the logistics of hydroxide, electron, reactant, and product transport. The CL microstructure will be constructed during the solvent volatilization, as an effect of accumulation of the catalyst/ionomer agglomerations (hereinafter referred to as agglomerates) [34]. The process conditions for the electrode preparation will make a great impact on the electrode structure and TPBs.

3.1. Effect of ionomer content on the electrode microstructure and single cell performance

Firstly, the electrodes incorporated with the varied contents of the alkaline ionomer AS-4 were fabricated and explored. In this work, the x value of the prepared CCM-Ix electrode ($x = 10, 15, 20$ and 25) was defined according to the mass ratio of the ionomer in CLs, by the following equation:

$$x = \frac{m_{\text{ionomer}}}{m_{\text{ionomer}} + m_{\text{catalyst}}} * 100 \qquad (1)$$

where m is the mass of the electrode material measured by weighting. Meanwhile, to prepare CCMs, IPA was selected as the dispersion solvent for the ionomer and Pt/C particles.

3.1.1. Microstructure of the catalyst layers

Fig. 2 exhibits the representative SEM images of the fabricated CCMs with 10–25 wt.% ionomer contents. It can be clearly observed that the size of agglomerates in the CL obviously increases with the increased ionomer content. Especially for CCM-I25 with the 25 wt.% ionomer content, the Pt-based catalysts are highly shielded and the pores on the surface are heavily blocked, which will hamper the electron, water and gas transport, and thus cause diminutions both in the active area and catalyst utilization. The resulting phenomena can be attributed to the ionomer incorporation into CLs serving not only as an interface material to extend the TPBs, but also as a binder to bind the catalyst particles to maintain the cell long-term run.

The pore structure of the prepared CCMs was measured by the MIP method. For comparison, a CCM-I0 sample without the AS-4 ionomer was prepared via the same procedure. The MIP results listed in Table 1 confirm that with the ionomer content increase, the cumulative pore volumes of these tested electrodes drop sharply from 0.589 $\text{cm}^3 \text{ g}^{-1}$ to 0.143 $\text{cm}^3 \text{ g}^{-1}$. The mean pore diameter and median pore diameter of these samples enlarges from 26.0 to 82.2 nm and 53.3–84.2 nm, respectively, resulting from the incorporation of the increased ionomer content. Compared with CCM-I0 and CCM-I10, the CCM-Ix ($x = 15, 20$ or 25) electrode with
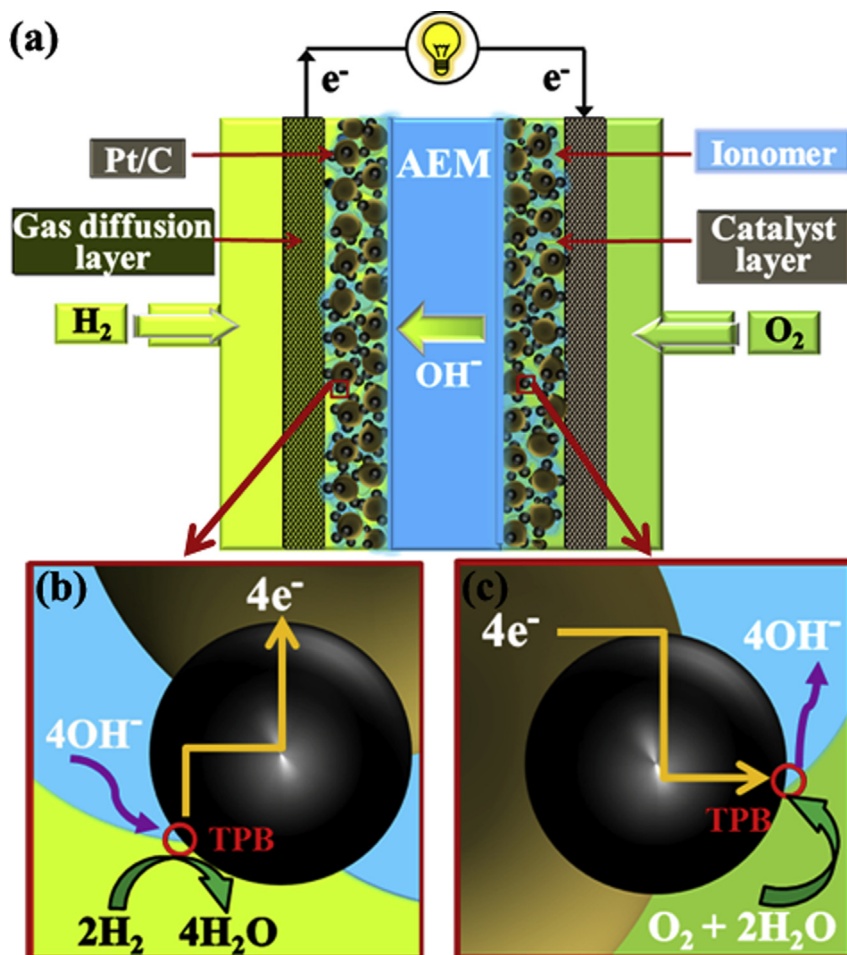

Fig. 1. Schematic illustration of (a) an AAEMFC, (b) the three phase boundary in the anode and (c) the three phase boundary in the cathode.
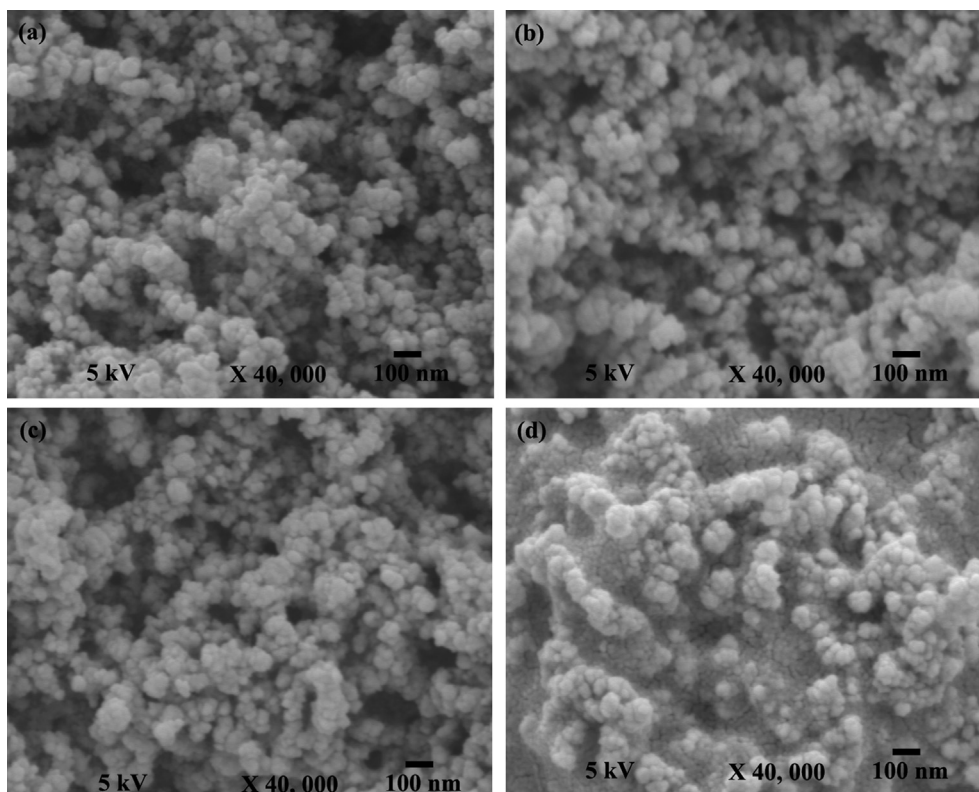
Fig. 2. SEM images of surface morphology of the CCMs at different ionomer contents, including (a) 10 wt.%, (b) 15 wt.%, (c) 20 wt.% and (d) 25 wt.%.

the high ionomer content obtain a smaller difference between the mean pore diameter and median pore diameter, confirming that the pores in CL tend to form the uniform median pores.

3.1.2. Single cell analysis

The home-made CCMs with the varied ionomer contents were subsequently assembled and investigated in fuel cells. The typical $i-V$ curves and power density curves are presented in Fig. 3. The electrode performance is commonly evaluated and compared according to the peak power density in AAEMFCs. The cell results show that CCM-I20 generated the highest performance with the peak power density of 358 mW cm^{-2} at 50 °C, which is about five and three times of CCM-I10 and CCM I25, respectively. It is thus confirmed that the alkaline ionomer only with the adequate content in the CLs will form the continuous network for aiding the hydroxide transport, correspondingly enlarging the reactive TPBs and enhancing the catalyst utilization. Whereas, the overloading ionomer will result in high shielding of electrocatalysts, heavy blocking of surface pores, regarding the H$_2$ and O$_2$ in the process of achieving the electrocatalyst particles for carrying out the electrode reaction.

For further analysis, the electrode kinetic characteristic parameters were obtained by fitting the $i-V$ curves above 0.75 V against a theoretical model as follows [32,35,36]:

$$E = E_0 - b \log i - Ri \tag{2}$$

$$E_0 = E_r + b \log i_0 \tag{3}$$

where, E_r is the reversible potential taken to be 1.22 V for H$_2$ + 1/2O$_2$ → H$_2$O under the experimental conditions [37], b is the Tafel slope, i_0 is the exchange current density, and R is the overall contributions of the linear variation of E with i, containing the ohmic resistance, charge-transfer resistance of the hydrogen oxidation,
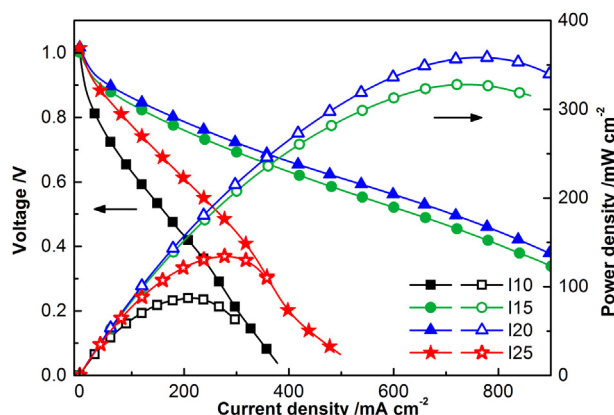
Table 1
Microstructure parameters of the CCMs at different ionomer contents.

CCM	Cumulative volume/cm^3 g^{-1}	Mean pore diameter/nm	Median pore diameter/nm
CCM-I0	0.589	26.0	53.3
CCM-I10	0.545	48.7	84.4
CCM-I15	0.250	74.7	73.1
CCM-I20	0.154	54.0	70.9
CCM-I25	0.143	82.2	84.2

Fig. 3. $i-V$ and power density curves of the single cells at different ionomer contents.

and mass-transport resistance in the intermediate current density region.

The combination from the fitted results (as presented in Table 2) and Tafel plots after *iR*-correction in Fig. 4, indicates that the ionomer content in CLs has significant effects on the electrode kinetic features in the whole studied current density window, including the activation, ohmic and mass diffusion polarization regions. The open circuit voltage (V_{OCV}) increases by about 20 mV when the ionomer content increases from 10 wt.% to 25 wt.%, as an indicative of decreased gas crossover. At the low current densities, the characteristic logarithmic shape of the *i−V* curve is primarily determined by activation polarization. The fitted Tafel slopes ranged from 26.7 to 51.3 mV dec^{-1} decrease in the order of CCM-I10 > CCM-I25 > CCM-I20 > CCM-I15, which inherently reflects the minimized activation barrier of the electrode reaction. The variety of slopes mainly originates from a change in the ionomer coverage on the catalyst particles due to the varied ionomer content in CLs, which influences the electrical work related to the electron transfer and the fractions of the total electrical potential difference at the catalyst/ionomer interface involved in the charge transfer process [32,33]. Meanwhile, the corresponding exchange-current-density i_0 based on the actual reaction zones presents an opposite tendency of the Tafel slop. It is surprised that there is 2-4 orders of magnitude change for i_o caused by the different ionomer loadings in CLs. Especially, CCM-I15 obtains the lowest i_o as an indication of the smallest reaction zones (i.e. TPBs) within its CLs. The i_o value for CCM-I10 is similar in magnitude to the previous results found in the publication [37], although the different methods are applied to fit the Tafel curves.

When current density increases, the shape of the *i−V* curve becomes approximately linear, and the deviation from the linearity appears in the Tafel plots, reflecting the effect of ohmic losses. This is caused both by the resistance due to the migration of hydroxide ions within the AEM and ionomer and by the resistance due to the electron flow. From the Tafel plots, it can be further observed that the onsets of the deviations from the linearity occur at the relatively lower current densities (around 20−30 mA cm^{-2}) for CCM-I10 and CCM-I25 in comparison with CCM-I15 and CCM-I20, arising from the increased ohmic polarization losses. This is well affirmed by the high-frequency resistance R_{HF} recorded via the above-mentioned electric load system. That is to say, when the ionomer content is less than 20 wt.%, the ionic resistance will be predominant due to the incontinuity of the ionomer network; while the electronic resistance will be predominant for the too much ionomer (e.g. 25 wt.%), since the As-4 ionomer is to the electron nonconductor.

With the current density further increased, the *i−V* curve begins to bend down, corresponding to the increased Tafel slops, originating from mass diffusion overpotentials for the limitations in the availability of reactants at TPBs. Actually, the reactant diffusion limitations for CCM-I25 can be clearly observed at the lower current densities as shown in Figs. 3 and 4, which can be taken as a major justification for its poor cell performance. The fitting result of *R* integrated with R_{HF} reflects the resistance characteristics of the electrode structure. It shows that the values of *R* and R_{HF} change in the same order of CCM-I10 ≫ CCM-I25 > CCM-I15 > CCM-I20. The ratio of R_{HF} to *R* (from 0.13 to 0.08) decreases gradually with the
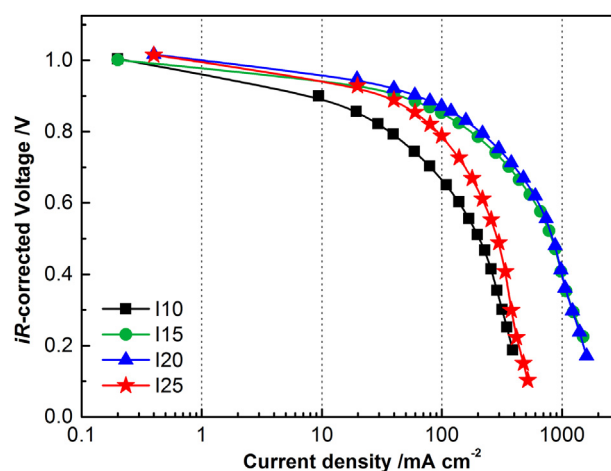

Fig. 4. Tafel plots of single cells at different ionomer contents.

increase of the ionomer content in CLs, indicating that besides electrode ohmic polarization, some other contributions to *R*, such as mass diffusion losses, have descended with the augmentation of the ionomer content.

The EIS is a useful tool to in-situ check and understand the separate voltage loss performance determining the overall fuel cell performance [37]. Fig. 5 gives the EIS spectra conducted at the current density of 100 mA cm^{-2}. It is noticed that the high-frequency resistance corresponding to the ohmic resistance increases in the same order of CCM-I10 ≫ CCM-I25 > CCM-I15 ≥ CCM-I20 as R_{HF}. In the meantime, the mass diffusion limitation inside the MEA can cause a double semicircle. These two arcs for the fuel cell process are defined as a medium-frequency feature and a low-frequency feature. The former represents the charge-transfer resistance of the electrode reaction, and the latter displays the resistance of the reactant mass transport [37]. According to the EIS spectra, CCM-I20 obtains the smallest arcs both in the mid-frequency and low-frequency regions in the fabricated CCMs, suggesting the enhanced catalytic activity and decreased mass transport losses due to the improved TPBs and electrode microstructure. For CCM-I10, the low-frequency arc seems to have been overlapped by the colossal charge-transfer resistance, which may be responsible for the debased catalytic activity for the electrode reaction.

To further certify the function of alkaline ionomer, the in-suit CVs of H$_2$/N$_2$ atmosphere was shown in Fig. 6. A steady increase of current density was observed with the increased ionomer

Table 2
Electrochemical properties of single cells at different ionomer contents.

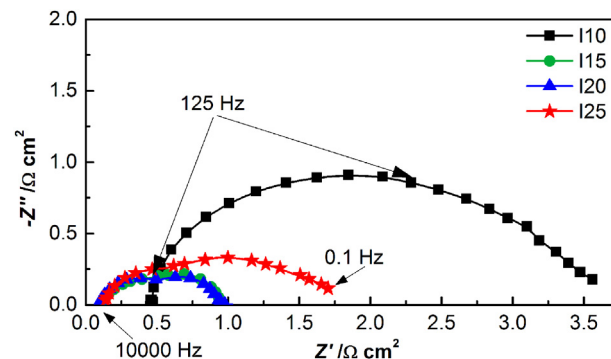| MEA	V_{OCV}/V	b/mV dec^{-1}	$i_o \times 10^{-10}$/A cm^{-2}	R/Ω cm^2	R_{HF}/Ω cm^2
CCM-I10	1.00	51.3	141	2.708	0.349
CCM-I15	1.00	26.7	0.0164	0.937	0.123
CCM-I20	1.02	33.7	4.36	0.775	0.093
CCM-I25	1.02	34.3	5.05	1.587	0.133

Fig. 5. In-situ EIS spectra of single cells at different ionomer contents. *Z′* is the real component of the impedance cell impedance vector; while *Z″* is the imaginary component.
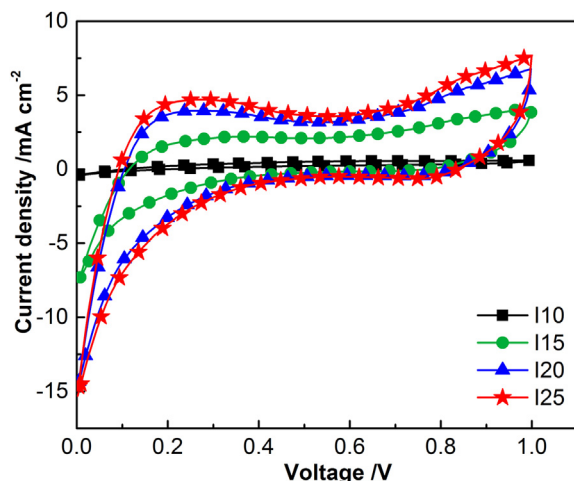
Fig. 6. CV curves of singles cells at different ionomer contents.

content in the testing voltage window, suggesting that the As-4 ionomer is indeed a strong hydroxide conductor, and the hydroxide transfer was correspondingly improved. Compared with CCM-I25, only slight changes of CV occurred in CCM-I20, which indicated that further increase of ionomer content (over 20 wt.%) would not considerably enhance the hydroxide conduction. Unlike in PEMFCs, the H_2 electrode with alkaline ionomer can produce an incredible influence on the cell performance, so comparative differences in CVs can be partly ascribed to the varied H_2 sides resulting from different ionomer contents. It is well known that the transport of hydroxide ions determined by the ionomer content is slower than that of H^+ ions, and the exchange current density of hydrogen oxidation reaction in alkaline is significantly lower than in acid. The latter is also crucial in relation to the cell i–V and Tafel curves above.

3.2. Effect of dispersion solvent on the electrode microstructure and single cell performance

Secondly, to investigate the impacts of the dispersion solvents in the catalyst slurry, CCMs with the 20 wt.% ionomer content in CLs were fabricated by employing different types of soluble solvents, containing EtOH, PA, IPA and n-butyl acetate (NBA), and subsequently marked as CCM-EtOH, CCM-PA, CCM-IPA and CCM-NBA, respectively. Some physical properties of these solvents are listed in Table 3. The commercial ionomer AS-4 as a quaternary ammonium hydroxide polymer could be highly solubilized in the $\varepsilon = 18.3$–24.3 solvents such as EtOH, PA and IPA, forming the solution state. Whereas, the ionomer AS-4 mixed with NBA ($\varepsilon = 5.01$) would form the colloid state structure, which was clearly identified by the Tyndall phenomenon as observed in Fig. 7. During the CCM preparation, the volatilization rates of solvents are favored in the

Fig. 7. Tyndall phenomenon of AS-4 in n-butyl acetate.

following order: IPA > EtOH > NBA > PA. It is important to point out that the selected solvents with low soluble. The viscosity of the $\varepsilon = 18.3$–24.3 solvents is in the range of 1.20–2.43 mPa s at 20 °C, and the less viscosity can be considered as a positive factor to enhance the fluidity of ionomers during evaporation.

3.2.1. Microstructure of the catalyst layers

Fig. 8 shows the SEM micrographs of prepared CCMs. Because of the volatilization and removal of the dispersion solvents, the catalyst particles and ionomer in the CLs tend to form agglomerates. The considerable difference of the CL surface morphology is observed in the SEM images, affirming the effect of dispersion solvents. For the $\varepsilon = 18.3$–24.3 solvents including EtOH, PA and IPA, the agglomerates size decrease as the following order: CCM-PA > CCM-EtOH > CCM-IPA. It reveals that the catalyst ink deposition progress requires a compromise between the ε and other properties like the boiling point, volatilization rate and viscosity, considering the fact that the solute-state ionomer appeared in these solvents. Particularly, the loose agglomerates of CCM-NBA leap larger particles, and the continuity for the ionomer network is thus improved, mainly ascribing to the solution-colloid state transition of the alkaline ionomer with the ε decrease of solvents.

The MIP results of the fabricated CCMs are listed in Table 4. It can be found that the cumulative pore volume of the CCMs made by solution method tends to increase as a result of the varied ε, boiling points, volatilization rates and viscosities of the dispersion solvents. More precisely, the CCM-IPA has around two and five times cumulative pore volume of the CCM-EtOH and CCM-PA, respectively. Whereas, the cumulative pore volume of CCM-NBA (0.123 m^3 g^{-1}) is close to that of CCM-IPA (0.154 m^3 g^{-1}). The mean pore diameter (13.9–76.5 nm) and median pore diameter (39.2–85.5 nm) of the CCMs increase in the order: CCM-NBA > CCM-IPA > CCM-EtOH > CCM-PA, demonstrating the colloidal method would

Table 3
Physical parameters of various dispersion solvents.

Solvent	Dielectric constant (ε)[a]	Boiling point /°C	Relative volatilization rate[b]	Viscosity[a] /mPa s
EtOH	24.3	78.4	1.4	1.20
PA	21.8	97.2	0.9	2.26
IPA	18.3	82.5	1.5	2.43
NBA	5.01	126	1.0	0.45

[a] Values obtained at 20 °C and atmospheric pressure.
[b] Contrasted to NBA at 25 °C and atmospheric pressure.
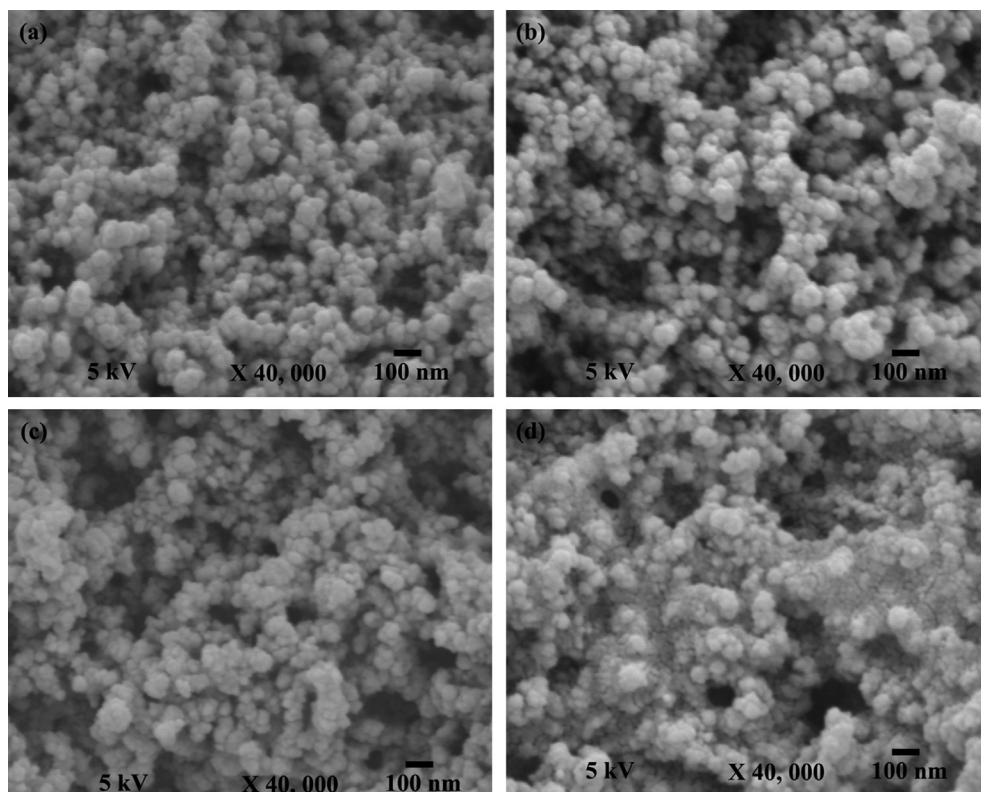
Fig. 8. SEM images of surface morphology of the CCMs using various dispersion solvents, including (a) EtOH, (b) PA, (c) IPA and (d) NBA.

remarkably enlarge the size of pores in CLs. Moreover, for CCM-NBA, the reducing difference between mean pore diameter and median pore diameter hints that the producing CL forms uniform large median pores. It has been investigated that the increased pore volume, especially those with the <100 nm diameter pores, was favorable not only for the mass transport losses but also for enlarging the active reaction zones [26].

Regarding the ionomer states adjusted by the solvent' ε, Fig. 9 gives the schematic diagrams of the CL formation during the CCM preparation. When the catalyst inks sprayed on AEMs heat up on a hot plate, the AS-4 ionomer is condensed due to solvent evaporation. According to the above SEM and MIP results, the formation of CLs may be in the following manner: for the catalyst ink fabricated using the solution method, the anion-exchange ionomer either deposits on the Pt/C particles or aggregates in the bulk liquid, and the fluidity of the catalyst particles is lost before the agglomerates are packed densely. Because the AS-4 ionomer in the solution form can be well dispersed with the $\varepsilon = 18.3$–24.3 solvents, and the space between the catalyst particles can be occupied by the ionomer, yielding CLs have many small agglomerates and pores. The MIP results indicate that the deposition of the ionomer on the catalyst particles is favored in the order: IPA > EtOH > PA, caused by the different physical properties of the dispersion solvents, like

dielectric constant, evaporation rate and viscosity. High viscosity is essential to maintain a catalyst ink suspension. Considering the IPA solvent with a high volatilization rate, the decreased fluidity of the catalyst ink for its high viscosity provides an advantaged condition to generate the CLs with the large agglomerates and high cumulative pore volume and large pore diameter (<100 nm). By contrast, for the colloidal approach using NBA with a small ε of 5.01, the ionomer with the poor fluidity tends to deposit on the electrocatalyst surface, and the ink agglomerates together during the solution volatilization, resulting in the fabricated CLs with the large and uniform agglomerates and pores, and forming good networks of the alkaline ionomers as seen in Fig. 8(d). Therefore, one can conclude that the TPBs created by the colloidal method are efficiently extended.

3.2.2. Single cell analysis

The test results of single AEMFC performance are given in Fig. 10. It shows that at the same ionomer level, the cell performance strongly depends on the dispersion solution for the catalyst ink. The peak power density decreases in the following order: CCM-NBA > CCM-IPA > CCM-EtOH > CCM-PA, matching well with the variety of their cumulative pore volume and pore diameter. It is thus confirmed the improved TPBs resulting from the enlarged catalyst-ionomer agglomerates, the optimized pore structure and the continuous ionomer network, and accordingly, the enhanced cell performance.

Especially, as shown in Fig. 11, there is a steady increase of the peak power density with the solvent's ε decrease, though the CCM-PA obtains the lowest performance which can also be taken as a result from some other properties of PA, such as its relatively high boiling point and low volatilization rate. According to the recorded R_{HF}, ohmic resistances in fuel cells reduce by about 29.4% when the solvent' ε values are decreased from 24.3 to 5.01. The peak power

Table 4
Microstructure parameters of the CCMs using various dispersion solvents.

CCM	Cumulative volume/cm^3 g^{-1}	Mean pore diameter/nm	Median pore diameter/nm
CCM-EtOH	0.071	32.0	61.7
CCM-PA	0.029	13.9	39.2
CCM-IPA	0.154	54.0	70.9
CCM-NBA	0.123	76.5	85.5

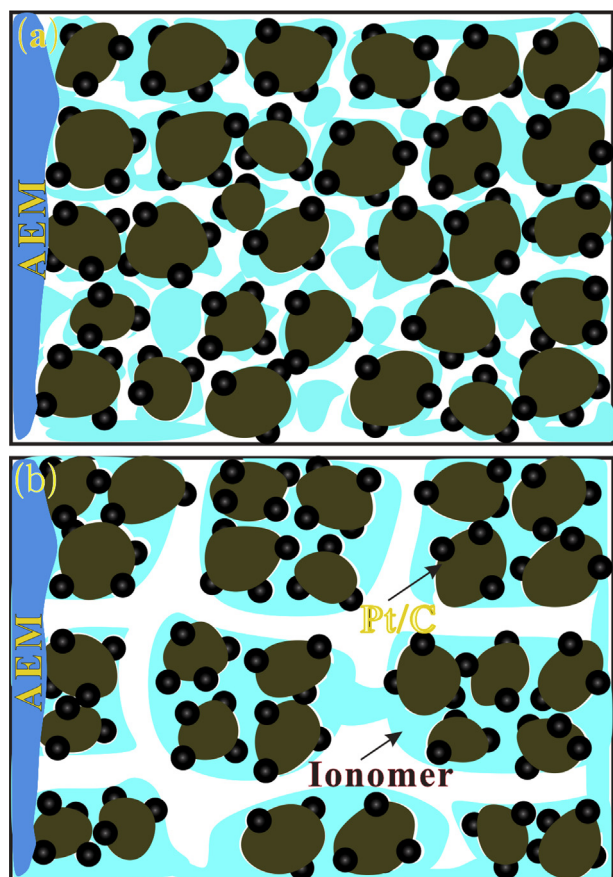**Fig. 9.** Shematic illustration for the CCM preparation using (a) the solution method and (b) the colloid method.

Fig. 11. Peak power densites of single cells versus the dielectric constant of each dispersion solvent.

A201 membrane, AS-4 ionomer, ca. 0.4—0.5 mg cm^{-2} Pt and 50 °C, etc [38].

For the analysis purpose, the electrode kinetic parameters were also obtained by fitting the $i-V$ curves at above 0.75 V as presented in Eq. (1) and Eq. (2). Associating with the Tafel plots (Fig. 12) after the iR-correction, the fitting results, Table 5, indicate that the Tafel plots in the low current density region and these parameters including V_{OCV}, b and i_o, are almost identical, revealing that the studied dispersion solvents have similar effects on the active polarization losses. In the high current density region, a sharp distinction is observed owing to the different ohmic overpotential and mass diffusion polarization losses. As for R, CCM-IPA obtains the highest performance, hinting the largest ohmic resistance. In contrast to the solution-method electrodes, the colloidal CCM-NBA shows a conspicuous advantage especially in the >700 mA cm^{-2} current densities, ascribing to its improved microstructure which can provide flexible reactant and product transport channels.

To further investigate the effect factors for the CCM performance, the in-situ EIS measurements were carried out at the current density of 100 mA cm^{-2} where CCM-EtOH, CCM-IPA and CCM-NBA were detected with the very similar $i-V$ performance (refer to Fig. 10). Compared with the results from various ionomer contents (Fig. 5), the EIS data, in Fig. 13, reveal that dispersion solvents only make slight effects on the high-frequency and mid-frequency

densities of the AAEMFCs with CCM-x (x = EtOH, PA, IPA and NBA) are 321, 220, 358 and 407 mA cm^{-2}, respectively. These observation indicates that the dispersion solvent' ε as a crucial parameter has a dominant influence on the CL microstructure and the resulting performance in AAEMFCs. Meanwhile, it is worth pointing out that the highest cell performance we achieved via the colloidal method is remarkable, compared to the performance for AAEMFCs known at present [24,32,38]. For instance, one of the best performance for AAEMFCs reported from Tokuyama Corp. was 250 mW cm^{-2} at the peak power density under the parallel conditions, including the
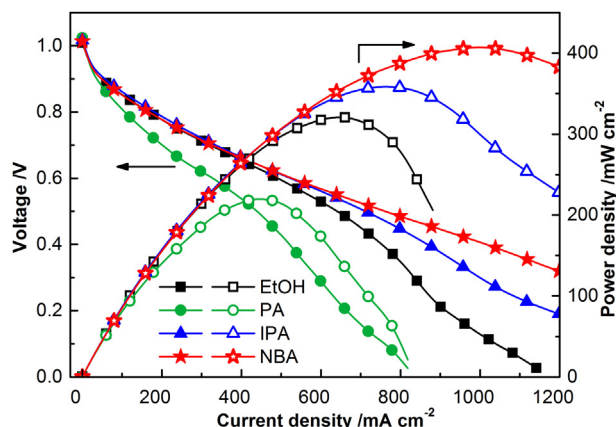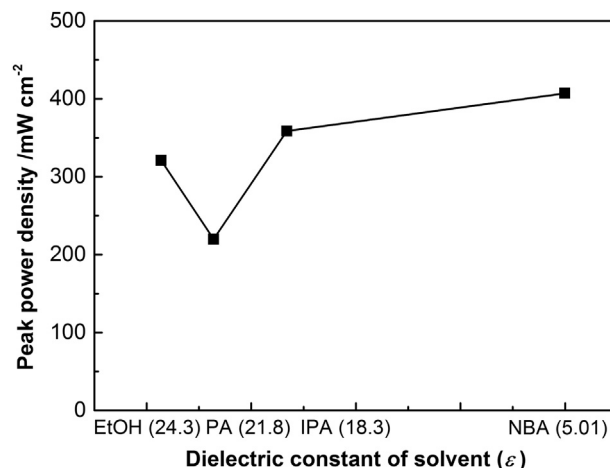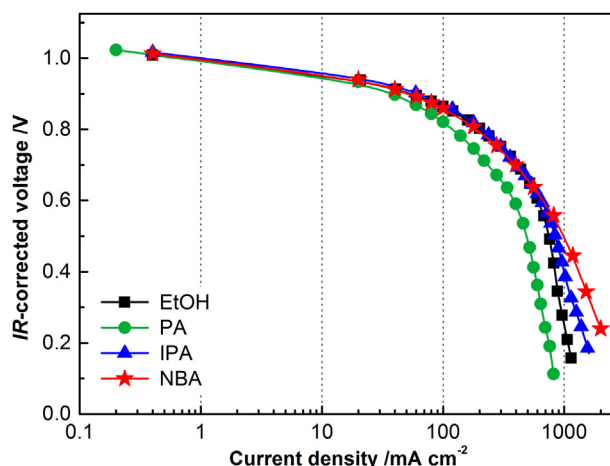

Fig. 10. $i-V$ and power density curves of single cells using various dispersion solvents.

Fig. 12. Tafel plots of single cells using various dispersion solvents.

Table 5
Electrochemical properties of single cells using various dispersion solvents.

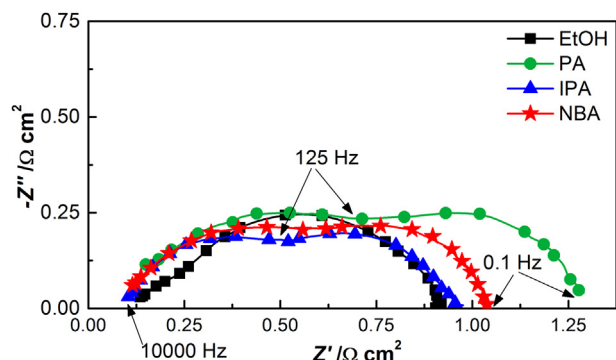| MEA	V_{OCV}/V	b/mV dec^{-1}	$i_0 \times 10^{-10}$/A cm^{-2}	R/Ω cm^2	R_{HF}/Ω cm^2
CCM-EtOH	1.01	33.7	2.54	0.791	0.126
CCM-PA	1.02	35.4	6.77	1.220	0.124
CCM-IPA	1.02	33.7	4.36	0.775	0.093
CCM-NBA	1.01	34.9	5.53	0.854	0.089

Fig. 13. In-situ EIS spectra of single cells using various dispersion solvents. Z' and Z'' see Fig. 5.

resistance referred to the ohmic polarization and charge-transfer limitations, reflecting the similar ohmic and active polarization losses at the studied current density. The main differences lie in the low-frequency region, corresponding to the mass-diffusion limitation. Therefore, it seems that the poor performance of CCM-PA can be mainly ascribed to the sharp increase of the mass-diffusion polarization losses.

4. Conclusions

Here, high performance electrodes for AAEMFCs with fine microstructure were successfully fabricated by adjusting the anion-exchange ionomer content in CLs and selecting the proper dispersion solvent for the catalyst ink. The ionomer was in-suit certified as a strong hydroxide conductor by the cell CVs. The ionomer content had synergetic effects on the electrode microstructure and kinetic properties in terms of the active, ohmic and mass diffusion polarizations. The prepared CCM-I20 with the 20 wt.% ionomer content showed an optimal power density of 358 mW cm^{-2} at 50 °C, which was related to the improved pore structure, continuous ionomer networks for hydroxide conduction, flexible mass diffusion channels and enhanced catalyst utilization.

In addition, depending on the solvent' ε, the solute-ionomer inks in EtOH, PA and IPA and the colloidal-ionomer ink in NBA were acquired, respectively. Compared with the solute method for the CCM preparation, the colloidal method showed some considerable advantages for enlarging agglomerate size, pore volume and pore diameter in CLs, organizing continuous networks for the hydroxide, reactant, product and electron transport, and thus decreasing mass diffusion losses. The maximum peak power density we obtained from the colloidal CCM-NBA was 407 mW cm^{-2} at 50 °C, which indicated a remarkable progress compared to the results reported in publications. Therefore, the current work provides a promising approach to improve the electrode TPBs and corresponding performance, though the cell durability and the material cost should be still considered to broaden the applications of the NBA-colloidal method in AAEMFCs.

References

[1] Y.-J. Wang, J. Qiao, R. Bakerb, J. Zhang, Chem. Soc. Rev. 42 (2013) 5768–5787.
[2] M.A. Hickner, A.M. Herring, E.B. Coughlin, J. Polym. Sci. B Polym. Phys. 51 (2013) 1727–1735.
[3] G. Merle, M. Wessling, K. Nijmeijer, J. Membr. Sci. 377 (2011) 1–35.
[4] J.R. Varcoe, R.C.T. Slade, E. Lam How Yee, Chem. Commun. (2006) 1428–1429.
[5] J. Pan, C. Chen, L. Zhuang, J. Lu, Acc. Chem. Res. 45 (2012) 473–481.
[6] É. Agel, J. Bouet, J.-F. Fauvarque, H. Yassir, Ann. Chim. Sci. Mat. 26 (2001) 59–68.
[7] I. Kruusenberg, L. Matisen, K. Tammeveski, J. Nanosci. Nanotechnol. 13 (2013) 621–627.
[8] P.A. Christensen, A. Hamnett, D. Linares-Moya, Phys. Chem. Chem. Phys. 13 (2011) 5206–5214.
[9] K. Matsumoto, T. Fujigaya, H. Yanagi, N. Nakashima, Adv. Funct. Mater. 21 (2011) 1089–1094.
[10] H. Meng, P.K. Shen, Electrochem. Commun. 8 (2006) 588–594.
[11] J. Pan, S.F. Lu, Y. Li, A.B. Huang, L. Zhuang, J.T. Lu, Adv. Funct. Mater. 20 (2010) 312–319.
[12] J.-H. Kim, S. Yonezawa, M. Takashima, Int. J. Hydrogen Energy 35 (2010) 8707–8714.
[13] H. Bunazawa, Y. Yamazaki, J. Power Sources 182 (2008) 48–51.
[14] H. Kim, J. Zhou, M. Ünlü, I. Anestis-Richard, K. Joseph, P.A. Kohl, Electrochim. Acta 56 (2011) 3085–3090.
[15] Y.B. Kim, T.P. Holme, T.M. Gur, F.B. Prinz, Adv. Funct. Mater. 21 (2011) 4684–4690.
[16] D. Kubo, K. Tadanaga, A. Hayashi, M. Tatsumisago, J. Power Sources 222 (2013) 493–497.
[17] B. Bladergroen, H. Su, S. Pasupathi, V. Linkov, Overview of Membrane Electrode Assembly Preparation Methods for Solid Polymer Electrolyte Electrolyzer, 2012.
[18] S. Litster, G. McLean, J. Power Sources 130 (2004) 61–76.
[19] A. Lindermeir, G. Rosenthal, U. Kunz, U. Hoffmann, J. Power Sources 129 (2004) 180–187.
[20] Y. Wanga, K.S. Chen, J. Mishler, S.C. Cho, X.C. Adroher, Appl. Energy 88 (2011) 981–1007.
[21] E. Passalacqua, F. Lufrano, G. Squadrito, A. Patti, L. Giorgi, Electrochim. Acta 46 (2001) 799–805.
[22] H. Gharibi, M. Javaheri, M. Kheirmand, R.A. Mirzaie, Int. J. Hydrogen Energy 36 (2011) 13325–13334.
[23] R.R. Passos, V.A. Paganin, E.A. Ticianelli, Electrochim. Acta 51 (2006) 5239–5245.
[24] Y. Zhao, H. Yu, D. Yang, J. Li, Z. Shao, B. Yi, J. Power Sources 221 (2013) 247–251.
[25] K.A. Sung, H.-Y. Jung, W.-K. Kim, K.-Y. Cho, J.-K. Park, J. Power Sources 169 (2007) 271–275.
[26] M. Chisaka, E. Matsuoka, H. Daiguji, J. Electrochem. Soc. 157 (2010) B1218–B1221.
[27] S. Gu, R. Cai, T. Luo, Z.W. Chen, M.W. Sun, Y. Liu, G.H. He, Y.S. Yan, Angew. Chem. Int. Ed. 48 (2009) 6499–6502.
[28] Y. Leng, G. Chen, A.J. Mendoza, T.B. Tighe, M.A. Hickner, C.-Y. Wang, J. Am. Chem. Soc. 134 (2012) 9054–9057.
[29] K. Ramya, G. Velayutham, C.K. Subramaniam, N. Rajalakshmi, K.S. Dhathathreyan, J. Power Sources 160 (2006) 10–17.
[30] J.-H. Kim, H.Y. Ha, I.-H. Oh, S.-A. Hong, H.-I. Lee, J. Power Sources 135 (2004) 29–35.
[31] H.-Y. Jung, J.-Y. Kim, J.-K. Park, Solid State Ionics 196 (2011) 73–78.
[32] M. Carmo, G. Doubek, R.C. Sekol, M. Linardi, A.D. Taylor, J. Power Sources 230 (2013) 169–175.
[33] D.S. Gnanamuthu, J.V. Petrocelli, J. Electrochem. Soc. 114 (1967) 1036–1041.
[34] A.B. Bose, R. Shaik, J. Mawdsley, J. Power Sources 182 (2008) 61–65.
[35] J. Kim, S.M. Lee, S. Srinivasan, C.E. Chamberlin, J. Electrochem. Soc. 142 (1995) 2670–2674.
[36] G. Squadrito, G. Maggio, E. Passalacqua, F. Lufrano, A. Patti, J. Appl. Electrochem. 29 (1999) 1449–1455.
[37] J.R. Varcoe, R.C. Slade, G.L. Wright, Y. Chen, J. Phys. Chem. B 110 (2006) 21041–21049.
[38] K. Fukuta, in: 2011 Alkaline Membrane Fuel Cell Workshop, 2011. Virginia.